



BACHELORARBEIT

Software implementation of the quality assurance tool for magnetic resonance imaging distortion assessment

Betreuer:

*Ao.Univ.Prof. Dipl.-Ing. Dr.techn. Martin Gröschl
Institut für Angewandte Physik
Technische Universität Wien*

in Kooperation mit:

*Peter Küss, PhD
& Piotr Andrzejewski, MSc Eng
Department of Radiooncology
Medical University Vienna, AKH Vienna*

von:

David Blacher
1327545

Technische Physik
E033261

April 23, 2017

Unterschrift StudentIn

Kurzzusammenfassung

deutsch?

Abstract

english

Contents

1	Introduction	1
1.1	Photon - matter interactions	1
1.2	Radiobiology	4
1.2.1	The human cell	4
1.2.2	Effects of radiation	5
1.3	Imaging modalities	5
1.3.1	X-ray projection imaging	5
1.3.2	Computer Tomography - CT	7
1.3.3	Magnetic Resonance Imaging - MRI	10
1.4	External Beam Radiation Therapy	14
1.4.1	Role of CT	16
1.4.2	Role of MRI	16
1.5	Aim of this work	17
2	Material and methods	19
2.1	Scanners	19
2.2	Custom build phantom	19
2.2.1	Frame and rods	20
2.2.2	Rod fillings	22
2.3	Sequences	24
2.4	Developed software tool	25
2.4.1	Processing MRI and CT scans	25
2.4.2	Capabilities	27
2.4.3	Measuring distortion	27
2.4.4	Calculation: dice-coefficient (DC)	28
2.4.5	Calculation: center of mass (COM)	28

3	Results	31
3.1	Obtained MRI and CT scans	31
3.2	Tested solutions	34
3.2.1	Visibility on CT/MRI scans	34
3.2.2	Mechanical properties of solutions	34
3.3	Distortion assesment	37
3.3.1	Distortion	37
3.3.2	DC	39
4	Discussion	43
4.1	Tested solutions	43
4.2	Distortion	43
5	Conclusion and Outlook	45
5.1	Preparing the phantom for distortion assesment	45
5.2	Future improvement of software tool	45
	Bibliography	47

1 Introduction

1.1 Photon - matter interactions

As light passes through matter, its intensity decreases. This phenomenon is due to photons interacting with electrons, nuclei, and their electric fields. All processes either change the direction they travels in, alter it's energy, or result in the disappearance of single photons. The probability of those interactions differ for each material (dependent on its density; proton number Z) and photon energy ($h\nu$).

If a photon's energy exceeds the binding energy of an orbital electron, the **photo-electric interaction** might occur. Also known as 'photo effect', it describes a photon being completely absorbed by a tightly bound orbital electron which then is ejected from its atom. The now free electron is called 'photo-electron'. Its kinetic Energy is the difference of the photons energy and the binding energy:

$$E_{kin} = h\nu - E_{binding} \quad (1.1)$$

Instead of being absorbed, photons might just 'bounce off' electrons or entire atoms, transferring momentum and in some cases a part of their energy to the electron. **Rayleigh (coherent) scattering** happens when a photon interacts with a tightly bound orbital electron (transferring momentum to the entire atom). This event can be seen as elastic, because only a negligible part of the photon's energy is transferred.

The **Compton effect (incoherent scattering)** involves a essentially free electron, such as an orbital electron with a relatively small binding energy compared to the photon's energy. Due to the weak binding, momentum is transferred only to the electron. This 'recoil electron' (or 'Compton electron') leaves its atom with a significant kinetic energy, which originated from the scattered photon. Since the photon loses part of its

energy, the event is considered inelastic.

When a photon with an energy above 1.02 MeV passes through the electric field of a nucleus, it might disappear to create an electron-positron pair. This effect is called **pair production**. The threshold of 1.02 MeV equals exactly the rest mass $E_m = 2m_e c^2$ for the two equally heavy particles. The new particles travel in opposite directions with the same kinetic energy

$$E_{kin} = \frac{h\nu - 1.02 \text{ MeV}}{2} \quad (1.2)$$

A photon with energy of the order of 2 MeV or higher can also interact directly with the nucleus. Such a **Photonuclear reaction** is similar to the photo effect, in the sense that the photon is completely absorbed. Its energy is transferred to the nucleus resulting in the emission of either a proton or neutron. [41, 27]

Attenuation

All those interactions result in a gradual decrease of light intensity as it travels through matter. The combined effect is described by **Beer's law**:

$$I(x) = I_0 e^{-\mu(h\nu, Z)x} \quad (1.3)$$

where x is the thickness of a homogeneous material and μ its linear attenuation coefficient. The different probabilities for the interactions to occur is implicitly considered by the attenuation coefficient $\mu(h\nu, Z)$ (see Figure 1.1 and 1.2).

For a photon being transmitted through matter with varying properties, the attenuation coefficient changes, too. After travelling a distance d , the intensity can be expressed as:

$$I(x) = I_0 e^{-\int_0^d \mu(x) dx} \quad (1.4)$$

Where $\mu(x)$ describes the attenuation at every distance x .

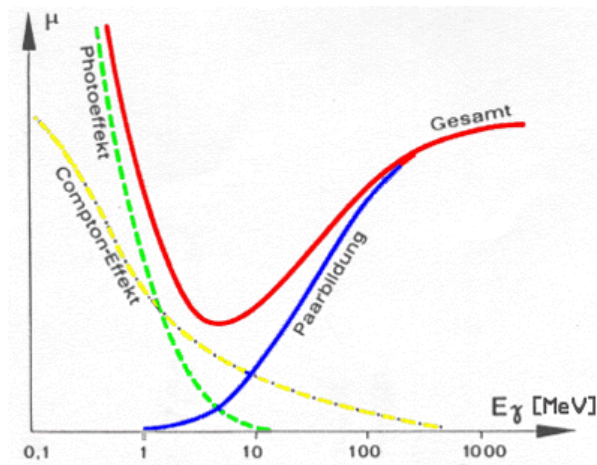


Figure 1.1: Photon attenuation schematic

http://www.onmeda.de/strahlenmedizin/ionisierende_strahlung_reichweite-schwaechungsgesetz,-reichweite-von-photonenstrahlung-2413-6.html

(TODO: better diagramm??) (TODO: explain LET? (linear energy transfer)) (TODO: explain 'dose'?)

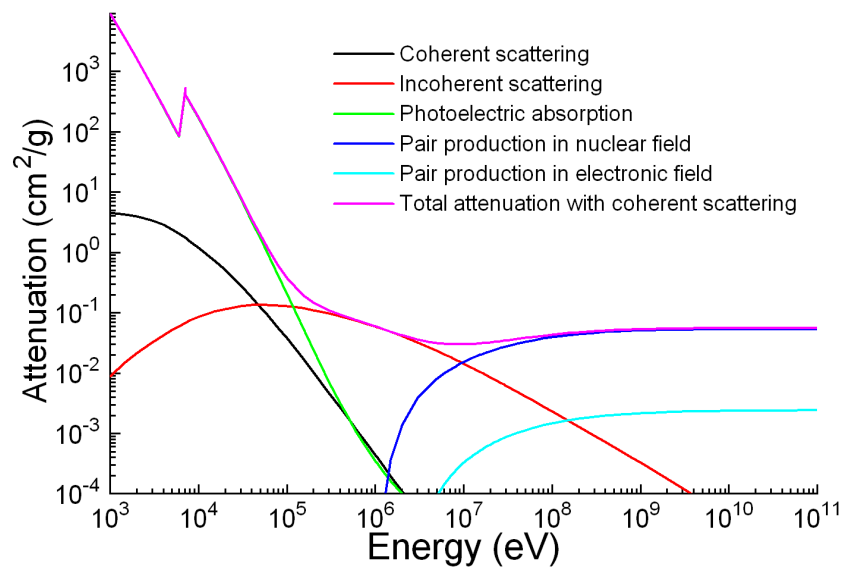


Figure 1.2: Photon attenuation for iron

<https://commons.wikimedia.org/wiki/File:Ironattenuation.PNG?uselang=en>

1.2 Radiobiology

1.2.1 The human cell

All living creatures consist of cells working together to form what is called tissue. A collection of tissues which perform one or more functions is considered an organ.

Even though different types of cells serve different causes, all of them originated from the same totipotent zygote containing a original set of DNA. A zygote is a stem cell, it has the ability to replicate indefinitely, passing on its DNA to the daughter cells. At the same time it can change into any type of body cell. This feature is why it is called 'totipotent'. As soon as the zygote has divided into a sufficient of identical cells, all of them differentiate into the various human tissues. In favour of becoming more specialised cells, they lose their totipotency. During the early stages of an embryo they are still capable of developing into a number of different cell types, but all within their own tissue type either nerve, skin or blood & muscle. As those cells further specialise, they limit their potential even more. In a fully grown human body there are still stem cells present, like bone marrow stem cells. Other than the zygote, bone marrow can only give rise to blood cells, but not to e.g. nerve or skin cells. A blood cell itself cannot replicate, it is considered a 'mature cell'.

The whole process follows the guidelines dictated by the DNA. Every cell inherited its own personal copy of the original set. Inevitably mistakes happen during the replication, resulting in changes to the DNA called 'mutation'. Most of these alterations are repaired or do not lead to changes in the cells behaviour. As the human body ages the repair mechanism slows down and mutations accumulate. At one point a cell is reprogrammed to act in a unpredictable way, giving up its duties and duplicating without restraint, forming tumours. External factors are known influence cell behaviour and able to induce such 'malign' cells (carcinogenesis). Cancer cells usually replicate more frequent than healthy cells, eventually leading to characteristic symptoms.

Different approaches have been developed to treat cancer, not all of which are suited to tackle every type of tumour. If the tumour's location is unknown or metastases in many places have formed already, chemotherapy might be considered. An easily accessible tumour could be removed in a surgery. Non invasive therapies also include radiotherapy, destroying cancer cells using radiation.

Generally, early treatments have high chances of success, but tumours are often

not noticed until they reached a certain stage. Reliable ways of diagnosing tumours are made possible by imaging techniques visualising the interior of the human body. [Baumann2017] (TODO: Citation needed! Or should I take it out completely?)

1.2.2 Effects of radiation

As described in 1.1, light passing through matter transfer some of its energy to the medium. Most interactions, such as the photo effect, incoherent (Compton) scattering, and pair production result in electrons being freed from their atoms. If the electron has a sufficiently high kinetic Energy, it may free additional orbital electrons from surrounding atoms. The remaining ions are positively charged, with a single unpaired valence electron. This type of chemical is called 'radical' and considered extremely reactive. They are likely to take part in chemical events which include the breakage of chemical bonds. Such processes can either induce changes in DNA sequences and eventually produce biological damage.

A irradiated cell can be affected in various ways ranging from no effect to cell death. The cell might survive containing a minor mutation. A more fundamental mutation might lead to carcinogenesis. Irradiated cells might send signals to their neighbours, inducing genetic damage known as 'bystander effects'. Cells have been observed to react to radiation, becoming more resistant to future irradiation.

Changes to the DNA might not become apparent ever, others take years until they result in biological effects. A well known consequence of ionizing radiation is leukaemia. Damage to germ cells (sperm and eggs) might even result in genetic damages expressed in subsequent generations.

While imaging modalities utilising X-rays are designed to apply as little dose as possible to keep effects of irradiation low, radiotherapy makes use of the lethal effects targeting cancer cells. [41, 27]

1.3 Imaging modalities

1.3.1 X-ray projection imaging

A widely used imaging technique based on photon interactions is X-ray projection. Its setup is made up by a light source, the object of interest, and a receptor. Since the technique is about projection, a patient needs to be placed between an X-ray tube and

the receptor (usually film-cassette or digital sensor). In the first stage of the imaging process, X-ray photons emitted by the tube enter the body. Next, while travelling through human tissue, they interact with its atoms in various ways (see 1.1). These processes govern how much light is absorbed or scattered. Finally, Photons which make it through the patient are recorded as they reach the receptor on the opposite side. This results in a negative greyscale image, where brightness values correspond to the intensity reduction. Low intensity (= high absorption) leads to bright spots on the image and vice-versa. The whole process could also be described as 'the projection of attenuation shadows on to the receptor', since the light absorption directly depends on the attenuation coefficient. The attenuation, on the other hand, depend on the tissue's properties (e.g. proton number Z , density, etc). Consequently, the attenuation shadows depict inner structures of the patient.

Soft tissue such as brain matter and muscles absorb only little light, casting a lighter shadow (dark areas on image) than bone which absorbs more photons (bright areas). Anything other than bone differs only slightly in attenuation, owing to the relatively small difference in atomic numbers and density. For this reason, X-ray projection imaging can be used to diagnose bone fractures, while at the same time it is not suited to clearly delineate soft tissue structures.

Other imaging modalities are better suited for the latter like medical ultrasound and Magnetic Resonance Imaging (MRI), to name a few. They are preferred for non invasive soft tissue examinations. If those imaging modalities are no option, X-ray projection can still be of some use in combination with contrast agents. Those substances fill e.g. the bloodstream with heavier atoms, which can be clearly seen against the dark background of surrounding soft-tissue. In CT angiography, for instance, iodine is administered intravenously enhancing vessel to vessel-wall contrast. In studies of the abdomen a diluted iodine solution or barium compounds swallowed by the patient leads improved visibility of the gastrointestinal tract.

For patients allergic to those chemicals, a number of alternative agents have been developed. Unfortunately most introduce slight, sometimes serious side-effects. There is ongoing research to find materials yielding enhanced contrast while at the same time minimising adverse reactions, a promising candidate being gold nanoparticles. [41, 27]

1.3.2 Computer Tomography - CT

Computer Tomography (CT) is a three-dimensional (3-D) imaging modality based on the measurement of X-ray attenuation. The technique has evolved from 2-D X-ray scanning. By mounting source and receptor on a rotary ring with a patient at the centre, projections from any angle can be obtained. However, in contrast to 2-D projection methods, the receptor resembles an arc made up by 800 to 900 neighbouring detector elements. A single 'image' taken by the receptor is therefore only in 1-D. Yet, by repeating this process from a sufficient number of different angles and along the entire patient (z-axis) a 3-D model can be computed. In contrast to 2-D methods, where the patients interior is projected/compressed onto a flat image, CT preserves the exact location information. This feature lead to a radical improvement in diagnostics.

Since its clinical introduction in 1971, CT has become a widely used 3-D imaging modality for a range of applications including radiation oncology. Especially in radiation therapy, knowledge of the exact geometry is crucial, which is why CT plays such an important role in treatment planning (see 1.4). [41, 27]

3-D image reconstruction

As a photon passes through the patient, it encounters different materials associated with characteristic linear attenuation coefficients. It is practical to think of the scanned body as a collection of $N = N_X \cdot N_Y \cdot N_Z$ finite size cubes (Δx cube length) called 'voxels' (analogous to pixels in a 2-D digital photograph). The entire model can then be regarded as a 3-D matrix, with the attenuation coefficients μ_i for all voxels as its entries. Figure 1.3 represents a (4, 4, 1) matrix. It depicts the path an X-ray may follow passing through voxels with different values μ_i . This discretisation allows us to change equation 1.4 to:

$$I(x) = I_0 e^{-\sum_{i=1}^{N_X} \mu_i \Delta x} \quad (1.5)$$

The initial and final intensities can be read of the settings of the X-ray tube and the detected signal. Based on those values, image reconstruction algorithms derive the three-dimensional linear attenuation coefficient matrix. For convenience the computed numbers are converted to Hounsfield Units, which are displayed in the final image. [41,

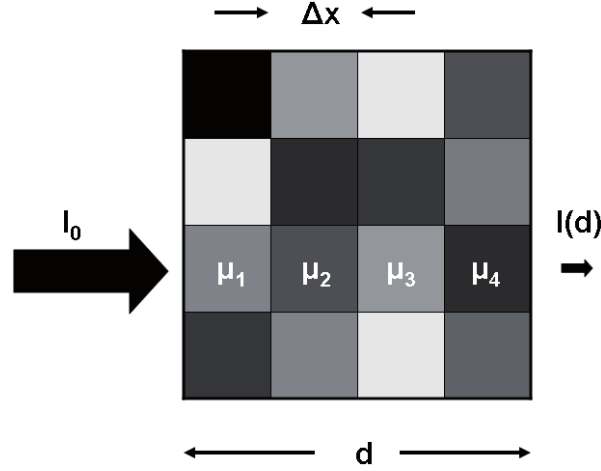


Figure 1.3: Simplified attenuation matrix (4,4,1)

Hounsfield Units

In a final CT scan voxel values are recorded in Hounsfield Units (HU), which relate to the attenuation of water at room temperature:

$$HU_{material} = \frac{\mu_{material} - \mu_{water}}{\mu_{water}} \cdot 1000 \quad (1.6)$$

Table 1.1 lists types of human tissue and their values on the HU scale. Generally HU values range from -1024 to +3071 (12 bit), but the upper limit can be extended to 15,359 (14 bit) if materials with even higher attenuation need to be visualised (e.g. implants).

Typically, CT scans are displayed on Computer monitors, which imposes the need to map the HU values to a 8-bit greyscale (256 steps of luminosity). Since the number of possible values (dynamic range) on the HU scale is 16 times the shades of grey on a screen ($12-8 = 4$ bit difference; equivalent to a factor of 2^4) the screen cannot convey all details at the same time. A linear mapping would result in 16 neighbouring values being compressed to the same brightness. This way, the brightest (bone) and darkest parts (soft tissue) of the image would be clearly distinguishable. At the same time small differences (<16 HU) would appear as exactly the same intensity. Generally however, the doctor's focus might lie either on soft tissue or bone material. Bearing in mind

Table 1.1: Average HU values for various types of human tissue

Substance	HU
Air	-1000
Lung	-750 (-950 to -600)
Fat	-90 (-100 to -80)
Water	0
Muscle	+25 (+10 to +40)
Brain, white matter	+25 (+20 to +30)
Kidneys	+30 (+20 to +40)
Brain, grey matter	+35 (+30 to +40)
Blood	+55 (+50 to +60)
Liver	+60 (+50 to +70)
Compact bone	+1000 (+300 to +2500)

that soft tissue values range only from 10 HU to 70 HU at most (see table 1.1), such a compression would make delineating organs using CT very unreliable. Instead of showing detail from the lowest to the highest value, a window of values can be chosen. Let's assume for example a range from -100 to 155 HU to be of interest. This selected range can be mapped directly and uncompressed to a 8-bit greyscale. Any values above 155 HU will be assigned the brightest value (white = 255), below -100 the darkest (black = 0). While showing very good soft tissue contrast, all bones would be depicted with exactly the same brightness (255), even though they might have a varying HU values. For bone structures a range from 300 to 2500 HU might show sufficient contrast. Standard computer programs used to display CT images allow the user to change the window interactively to any value range. [41, 27]

Image acquisition

The time necessary to collect 1-D attenuation projections from sufficient angles is called 'acquisition time'. In 2-D X-ray scanning only one picture is taken, while a 3-D CT model is made up of a photo sequence. If the patient moves during the imaging process, the final model would show motion artefacts which might lead to wrong conclusions. Consequently, CT scanners are designed to minimise acquisition time while ensuring sufficient image quality. Very fast CT protocols result in smaller resolution, because less images are taken. [41, 27]

Image quality

CT offers excellent low contrast resolution, making structures that differ only slightly in signal from their surroundings visible to doctors. This aspect of image quality is mainly limited by noise. Noise is random patterns underlying the actual signal which always present to some extent. It's prominence in the final image is described by the Signal to Noise Ratio (SNR). If the SNR is too low, fine structures blend with the noise and cannot be distinguished. Strategies to achieve a high SNR include raising the initial photon flux (intensity) or employing contrast agents. The intensity is governed by the tube current, which is limited by the heat capacity of the tube and health considerations regarding the patient.

Alternatively, the spatial resolution can be decreased, effectively combining neighbouring image slices. While SNR for combined slices is increased, fine structures along the z-axis might be lost due to the reduced resolution. [41, 27]

Health considerations

CT scans describe the attenuation throughout a patient, which is directly related to how much energy is transferred from photons to matter. Only because X-rays are absorbed by the human body, this imaging modality gives insight in the density distribution of a body's interior. However, this transferred energy is capable of causing biological damage. (see 1.2.2) Fortunately the radiation dose administered during a single CT scan is almost negligible. Nevertheless, cancer patients need to be imaged frequently during treatment planning. Especially children receiving a great number of CTs typically suffer from induced cancer occurring up to 40 years later. So while the benefit from using CT for diagnostics far outweighs the damage, there have been major efforts to reduce dose while maintaining reasonable image quality. [34, 5, 56, 55, 29, 16]

1.3.3 Magnetic Resonance Imaging - MRI

Magnetic Resonance Imaging (MRI) is a 3-D imaging modality based on Nuclear Magnetic Resonance (NMR), a phenomenon discovered by physicist Isidor I. Rabi in 1938. Atomic particles such as protons have an inherent quantum mechanic feature called 'spin', which is associated with a magnetic moment μ . Without an external field a proton's spin is oriented in a random direction in space and with it its magnetic moment. The sum of magnetic moments belonging to a great number of protons results in a net

magnetisation. Due to their random orientation, the net magnetisation will be zero measured from a great distance (in relation to the spins' distances). On average, for every proton's spin there is always another particle's spin oriented exactly the opposite way, cancelling its magnetic moment.

In the case of an applied external magnetic field, the spins will either align parallel or anti-parallel to the direction of this field, minimising their energy. Protons aligned parallel have a slightly lower energy than those looking the other way. In a collection of many spins, the number of parallel spins will therefore dominate, resulting in a net magnetisation greater than zero (see figure 1.4).

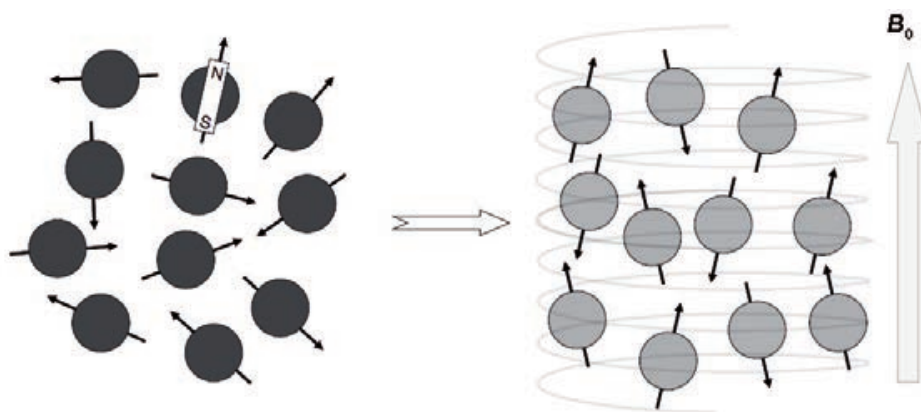


Figure 1.4: The spins, initially oriented randomly in space, become aligned either parallel or antiparallel to an externally applied magnetic field B_0 .

By applying a radio frequency pulse, the total external magnetic field changes and the magnetic moments start precessing around that new external field. The pulse duration is usually chosen in such a way it causes the spins to flip by a 90° angle. They are now oriented in the transverse plane to the original external field, and so is the resulting net magnetisation. Similar as to how a spinning top rotating at an angle to the direction of gravity precesses, the magnetic moments will now precess about the direction of the external field with a frequency linearly proportional to the external field strength. This precession movement can be detected, because the net magnetisation still follows their orientation. Again the particles would like to minimise their energy by aligning their spins with the external field, but in order to do so they need to give away the additional energy, transferring it to the surrounding lattice. Those spin-lattice interactions happen with different efficiency depending on the tissue. The amount of time it takes for the spins to align is expressed in a material specific time constant T_1 . Shortly after applying

the radio frequency pulse, regions of the body where magnetic moments align quickly (short T_1) have a stronger net magnetisation (in the direction of the external field) than those where energy is being transferred slowly (long T_2).

At the same time, the spins interact with each other, affecting the local magnetic field and spins in their vicinity. The magnetic moments, which started out precessing in phase directly after the radio frequency pulse flipped them, will precess at slightly different frequencies, because of the small fluctuations in local magnetic field. The differences cause the collection of magnetic moments to de-phase and the net magnetisation in the transverse plane to vanish. This process due to spin-spin interactions is described by the material specific time constant T_2

Eventually all spins will be again aligned either parallel or anti-parallel to the external field, just as they were before the rf-pulse. Applying the RF pulse with a homogeneous field strength along the body would excite all spins simultaneously. In order to localise differences in tissue magnetisation, the RF pulse is instead combined with a linear magnetic gradient field 'selecting' a slice to be imaged at a time. The rest of the body is unaffected, the signal measured after such a pulse comes only from the chosen slice.

Measuring the net magnetisation throughout the body can therefore give information about tissue differences. During a MRI scan procedure, the region of interest is surrounded by a pick-up coil measuring the net magnetisation. Doctors can choose to create images that reflect the spin-lattice interactions (T_1 weighted) or the spin-spin interactions (T_2 weighted). A set of imaging parameters/settings that influence the outcome of the scan are called 'image sequence'. Delineating tumours or lesions is often accomplished by looking at both T_1 and T_2 weighted images and drawing the right conclusions.

Soft tissue contains a lot of water, which is made up by Oxygen and Hydrogen. Hydrogen nuclei are the protons and their NMR is which MRI is tuned to make visible. This is why soft tissue appears as bright areas in MRI, whereas bone material has only little contrast. [10] Studies have shown that delineating certain types of tumours, for example prostate cancer, is more accurate using MRI images than using CT. [46, 12, 47] While in diagnostics MRI scans might be sufficient, radio therapy treatment planning needs more and other information about the regions surrounding the tumour. CT has other advantages which make it an essential part for external beam radiation therapy. (see 1.4)

Image Quality

(TODO: rewrite) Generally, diagnostics benefit from greater image quality. However, at some point diagnostic accuracy stops increasing with field strength. Nevertheless, high field scanners are key to developing new methods such as functional MRI (fMRI) of the brain [14] and observing “metabolic reactions occurring in a human body in addition to producing very precise images of body structures” [60]. At the same time astonishing improvements can be achieved at low fields. A “combination of field independent polarization [...] with frequency optimized MRI detection coils [...] results in low-field MRI sensitivity approaching and even rivaling that of high-field MRI.” [8]

Health considerations

Strong static magnetic fields up to $3T$ are present around MRI scanners at all times, and precautions are necessary to ensure safety for patients and medical personnel. Ferromagnetic materials (such as steel and iron) can become dangerous projectiles in vicinity of the MRI scanner. They must be excluded from the room containing the magnet without exception. Furthermore, medical implants including, but not restricted to cardiac pacemakers and hearing-aids might malfunction or become damaged in strong fields, regardless whether they contain ferromagnetic materials. Patients with such implants might still be imaged using scanners producing weak fields up to $0.5T$.

The RF pulses used to manipulate the local magnetisation repeatedly puts spins in excited states, transferring energy to the human body. MRI scanners are designed to limit the rise of a patient’s body temperature to $0.5^{\circ}C$ during standard imaging. Only with either medical or appropriate psychological monitoring the limit raises to $1^{\circ}C$ in body temperature. For any higher values a ethics committee approval is necessary. In general patients should be exposed to RF fields only as strong as their thermoregulatory system is capable to cope with.

To encode signal with a location, magnetic fields gradient are applied together with the RF pulse. They are switched at high frequencies leading to induced currents in conducting body tissue. In principle, those currents stimulate nerves which might result in muscle twitching or pain. However, gradient levels are set to avoid negative effects.

(TODO: incorporate following quote/source) "The HPA (2008) [15.4] has summarized the literature on the effects of low frequency time varying fields typical of those used in MRI. No consistent evidence of harm following short term exposures was found, although some subtle biological effects have been reported. Subjects with epilepsy or

who are taking drugs that reduce seizure activity may exhibit increased sensitivity to stimulation by electric fields induced in the cortex and should be imaged with caution."

Open bore MRI scanners

(TODO: rewrite) The radiation oncology department of the Vienna General Hospital (AKH) is equipped with an 0.35T open-bore, c-arm MRI scanner. The open design improves the well-being of patients experiencing anxiety in closed scanners. Consequently, the number of incomplete MR examinations due to claustrophobic events is low. [15, 3] Besides, patients who wouldn't fit in closed designed scanners can be imaged. Also, brachytherapy patients can be placed in the scanner with applicators attached.

This type of scanner is weaker than a conventional closed bore scanner (1-3 Tesla). High field strengths would result in greater resolution, better Signal to Noise (SNR) ratio, and faster imaging time. However, "There are definite cost advantages (capital, operating, siting) to the use of lower field MRI." [49] Permanent magnets are sufficient to create the 0.35T field. Therefore there is no need for constant cooling using liquid helium compared to superconducting magnets. Consequently, maintenance and service costs are considerably lower.

more stuff to be looked at

(TODO: incorporate into existing sections:) One drawback of MRI, and especially open bore scanners, is the occurring distortion due to inhomogeneities in the magnetic field. For most applications small position shifts and deformations are of minor importance. In RTTP however, those effects can have a big impact. Therefore MRI scanners usually come equipped with an internal distortion correction algorithm. Those methods are developed by the company designing the scanners. Knowing the technical details enables them to drastically reduce the distortion.

Field of view (FOV) of the MRI scanner is smaller than the CT scanner's.

1.4 External Beam Radiation Therapy

External Beam Radiation Therapy (EBRT) utilizes ionizing radiation to damage cancer cells in order to stop them from multiplying. This prevents the growth of tumours and eventually cures the patient. In conventional EBRT photons (x-rays) in the range

of 4MeV to 20MeV are used to administer the necessary dose at the location of the tumour. Unfortunately, photons interact with all cells they're passing through until they are fully stopped. They release their energy slowly while travelling through the patient and usually get completely absorbed after leaving the body. Charged particles (e.g. protons, carbon ions) minimize the damage done to healthy tissue due to their distinctive behaviour in energy loss called “Bragg Peak”. They release most of their energy shortly before stopping. [35] This effect can be used to spare tissue lying behind the tumour from radiation. [38] A comparison between x-rays and protons is shown in figure 1.5.

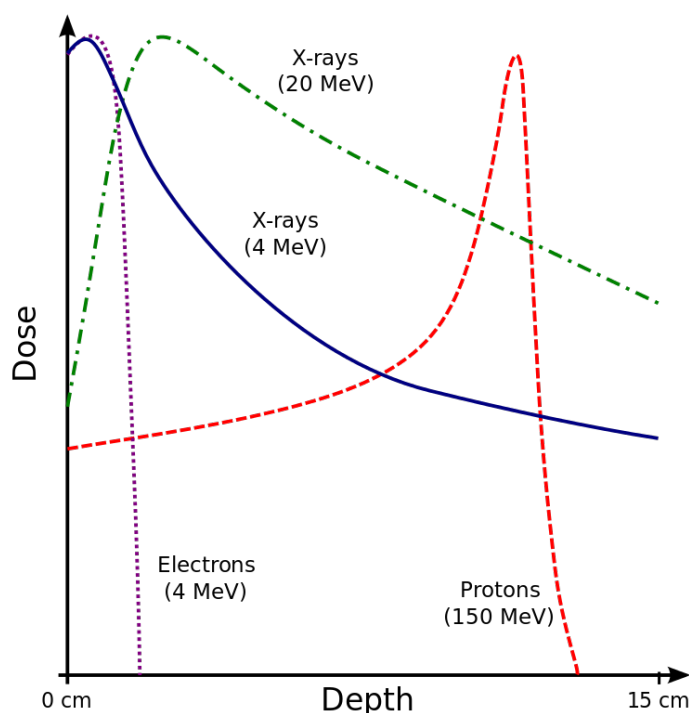


Figure 1.5: energy release of ionizing radiation
 (By Cepheiden, via Wikimedia Common;
 GFDL <http://www.gnu.org/copyleft/fdl.html>)

While travelling through matter both types of radiation release energy mostly due to coulomb interactions with the outer shell electrons of atoms. Knowing the electron density of the targeted tissue area is therefore essential. In order to reach a specific penetration depth, the particles' initial energy has to be chosen accordingly.

1.4.1 Role of CT

(TODO: rewrite)

Until recently radiotherapy treatment planning (RTTP) relied heavily on Computer Tomography (CT). There are two main reasons for this:

Firstly, CT uses low energy x-rays to create a 3D image of the patient. The luminosity value (brightness) assigned to each voxel (like pixel, but three-dimensional) corresponds to the local radiodensity recorded in Hounsfield units (HU). Materials with a higher radiodensity (e.g. bones) absorb more x-ray photons than those with less (e.g. water, brain-matter). Calculating the electron density using data obtained with CT is an easy task and used widely for RTTP. [9, 51] In order not to induce new cancer cells in healthy tissue during EBRT, the radiation beams are carefully targeted using the measured radiodensity. This way the absorbed dose accumulates in the cancer regions, while the nearby healthy tissue receives less radiation.

Secondly, CT images generate 3D images with little distortion. Exact geometries are needed for correct RTTP.

Image of RTTP

1.4.2 Role of MRI

(TODO: rewrite) There are some difficulties arising from combining CT and MRI for EBRT: In order to profit from separately acquired data, the resulting images must be aligned either manually or automatically. This is a hard task since non-rigid objects (organs) change their shape and location between measurements. This leads to inaccuracies. Therefore MRI-only radiation therapy protocols are being developed: MRI data is used to create a Pseudo-CT, which contains information about electron density.

Comparisons to using CT and MRI have shown acceptable deviations for X-ray therapy. In charged particle therapy the resulting dose gain in healthy tissue and dose loss in cancer regions due to inaccurately assigned electron density values is bigger. However, current development is promising. [45, 57, 36, 17, 7]

Today RTTP often combines CT images with data acquired using Magnetic Resonance Imaging (MRI). MRI scans also record luminosity values, but they do not correspond to HU (radiodensity measured by CT). The signal intensity depends on many factors and even varies between MRI scanners.

1.5 Aim of this work

The used open bore MRI scanner is not intended to be used for RTTP. The on board correction algorithm might not be good enough for effective EBRT. The goal of this work is to commence the development of a quality assurance tool to assess the spatial distortion (after applying the internal correction). This is achieved by comparing MRI images to CT images used as a gold standard. An already existing custom designed phantom is provided by the AKH Vienna for this purpose. However, the liquid to fill the rods with has not been chosen yet. Therefore, this paper focuses mainly on the acquired data and which liquids to use the phantom with, not its entire design. However, possible fillings have to be produced and tested. Similar approaches are being used for distortion correction by other facilities. [42, 39, 58, 62, 63, 33]

2 Material and methods

2.1 Scanners

CT and MRI scanners used during this work are listed in Table 2.1.

System	product name	company	coil [internal W x H]
MRI	Magnetom C!	Siemens	Body/Spine Array Coil XL [50 x 30.5 cm (19.7 x 12 in)]
CT			

Table 2.1: used scanners

2.2 Custom build phantom

To measure distortion the scanners must image a rigid object with known dimensions. Such phantoms are commercially available, but often expensive and designed for a specific calibration protocol. Some institutions build their own to fulfill exactly the requirements of a given application.

For the AKH it was important to create a lightweight phantom which can be imaged by CT and MRI scanners. Due to the underlying physics, only fluids are visible in MRI scans. CT however, also shows plastic. See figure 2.1 for a comparison (MRI/CT visibility). Therefore, they decided on plastic rods with a suitable fluid filling. Such a liquid should be easily produced, non-toxic, and yielding sufficient signal in MRI scans.

Commercially available phantoms often resemble water filled tanks containing plastic grids as a reference. This design results in stronger signal, but exceeds practical weight. There are few brands offering solutions utilising liquid fiducial markers in the shape of pellets. They are arranged in a regular pattern surrounded by air or plastic. The AKH's design however relies on replaceable rods, which makes it a novelty.

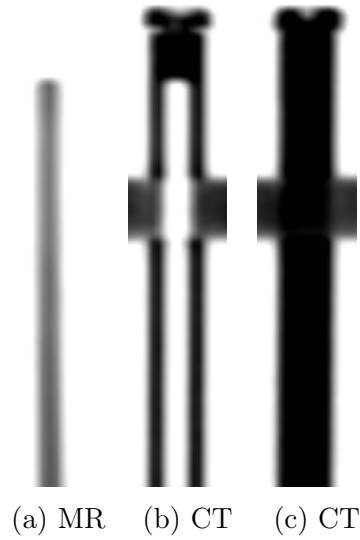


Figure 2.1: Comparison: MRI only shows liquid filling, CT also the plastic rod and pane (horizontal black bar crossing middle and right rod);
(a:) *MRI* - filled rod, plastic not visible (field of view too small to show entire rod); **(b:)** *CT* - empty rod, plastic visible; **(c:)** *CT* - filled rod, plastic and filling visible

2.2.1 Frame and rods

For the open-bore MRI scanner the phantom was build to fit exactly the scanner's coil. Three parallel acrylic glass panes in the shape of the coil serve as a rigid frame. In the middle an empty area was reserved for an optional additional smaller phantom (not used for this work). Figure ?? shows an picture of the phantom. See also figure 2.2 showing a CT image of one pane (with no rods inserted).

More than 300 plastic rods (length: 50cm, outer diameter: 8mm, inner diameter: 4mm, volume: approx. 6mL) could be placed in the phantom. See figure 2.3 for a schematic sketch. The bottom part of each rod was sealed with a hot glued plastic plug, the top could be closed with a plastic screw. Frame and rods were already build and assembled before the author started working on this project.



Figure 2.2: plastic pane, no rods inserted

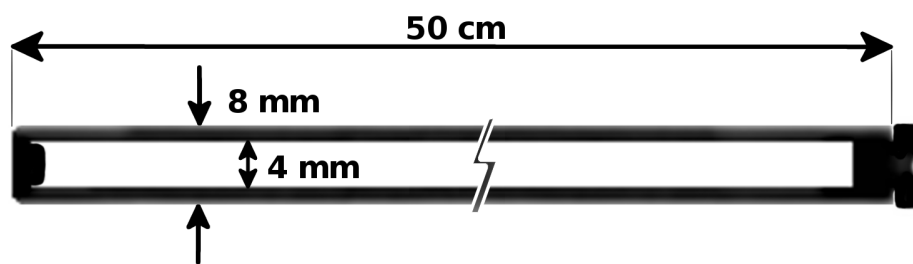


Figure 2.3: empty plastic rod, schematic (not true proportions);

photo of Phantom photo of single rod

2.2.2 Rod fillings

For this study 17 different liquids were produced to be tested as possible fillings. They are listed in Table 2.2.

Most tested fluids are based on water. This makes it easy to empty and clean the rods if needed. They could then be filled again with a different liquid. The chosen components are either non-toxic or harmless if not swallowed. Unfortunately the water might evaporate over time. To improve the mobility of trapped air bubbles, soap was added to some fluids.

As an alternative 2 oils were proposed. They do not contain water and air is not soluble in oil. Once a rod is completely with oil, no air bubbles should form. Using vegetable oil would be a non-toxic solution. This has been ruled out as a filling, because it would eventually rot. Mineral oil on the other hand does not rot.

Nr.	$NaCl$	$CuSO_4 \cdot 5H_2O$	Soap	Ascorbic Acid	Agar	Primovist [volume-%]
#1						
#2	3.6	1.96				
#3	3.6	3.92				
#4	3.6	19.6				
#5	3.6	1.96	1			
#6	3.6	1.96	5			
#7	3.6	1.96	20			
#8	3.6	1.96		0.36		
#9	3.6	1.96		3.6		
#10	3.6	1.96		36		
#11	3.6					0.1%
#12	3.6					1%
#13	3.6					10%
#14	3.6	1.96			0.5	
#15	3.6	1.96			20	
#16		Motor Oil:	<i>Castrol Power1</i>			
#17		Silicon Oil:	<i>Charge: 15HLVY023</i>			

Table 2.2: composition of tested solutions
(components in g/L ; exception: Primovist in volume%)

- #1 *distilled water* (as reference)
- #2 $NaCl + CuSO_4 \cdot 5H_2O$ (as suggested by AAPM MR Subcommittee [21])
- #3 increased concentration of $CuSO_4 \cdot 5H_2O$
- #4 further increased concentration of $CuSO_4 \cdot 5H_2O$
- #5 generic washing-up *soap* added to #2 (suggestion by Data Spectrum Corporation [11] to keep air bubbles from sticking to phantom walls)
- #6 increased *soap* concentration
- #7 further increased *soap* concentration
- #8 *ascorbic acid* added to #2 (reduce forming of air bubbles by binding dissolved oxygen. It then degrades to dehydro-ascorbic acid and water. [2, 4] Concentration of $0.36 g/L$ corresponds to approx. $0.00204 mol/L$)
- #9 increased *ascorbic acid* concentration
- #10 further increased *ascorbic acid* concentration
- #11 *Primovist* (a common contrast agent used for MRI scans [59, 48, 40])
- #12 increased amount of *Primovist*
- #13 further increased amount of *Primovist*

#14 *agar* (or agarose is commonly used as basic reference material for MRI phantoms [6, 28])

#15 increased *agar* concentration

#16 synthetic motor oil

#17 silicon Oil

Being closed at one end and having a capillary shape (small diameter) makes it impossible for the rods to be filled by pouring in the liquid. Instead of adding the fluid at the top, it has to be injected starting at the bottom. This way the contained air would be pushed out through the opening on the top. A thin plastic tube was used to leave room for the gas to escape. Between different liquids the tube was flushed with #1 (distilled water) or #2 (main component of most solutions).

In order to minimize the amount of gas dissolved, the liquids were brought to boil shortly before injecting. Gas solubility generally decreases with rising temperature [19, 50] After injecting the solution in the rods, they were left to cool down. Before closing the rods were topped up completely (no trapped air bubbles). The oil based liquids, #16 and #17, were not brought to boil. Number #14 could be injected without problems, the solution remained fluid even after reaching room temperature. Number #15 on the other hand changed to a gel like consistence and clogged the tube right after the rod was filled. The tube could not be used again.

2.3 Sequences

Following the suggestions given in the Report of AAPM MR Subcommittee TG1 “MR Acceptance Testing and Quality Control” [21], T1 weighted sequences were chosen to evaluate the possible solutions. (Table 2.3)

System	—	—	—	—
MRI	-	-	-	-
CT	-	-	-	

Table 2.3: used sequences

2.4 Developed software tool

In order to assess the distortion of the MRI scanner, a tool was programmed. It is written in Python 2.7 and uses the *SimpleITK* package to read and process *DICOM* (“*Digital Imaging and Communications in Medicine*”) files. [44, 13] *SimpleITK* is an object-oriented “C++ library with wrappers for Python, Java, CSharp, R, Tcl and Ruby”. [52, 54] Its versatility is one of the reasons why this approach was favoured. It is a simplified layer built on top of the National Library of Medicine Insight Segmentation and Registration Toolkit (ITK). SimpleITK is also used by Applications like *3D Slicer*, a “free and open source software package for visualization and medical image computing”. [1, 23] For this work 3D Slicer was used to crop images, quickly read values and visualize the results. Documentation and code examples of SimpleITK can be found at [53, 25] An alternative way to handle DICOM data in Python would be Pydicom. [43, 24]

An extensive list of packages used to process data:

- SimpleITK
- numpy
- scipy
- matplotlib.pyplot [20]
- skimage.draw
- datetime
- os

2.4.1 Processing MRI and CT scans

Prior to analysing their data, the scans had to be prepared. To start with, they were aligned in a way that yields maximum overlap especially in the centre of the image. However, the MRI image had a lower resolution than the CT scan. Therefore, the MRI voxel’s size were changed to match the CT voxels. Both images were resampled to CT resolution. Those steps were performed using *MIRADA* (?????).

As described later, resolution might influence the efficiency of the distortion assessment. The application *3D Slicer* (Version: Slicer-4.5.0-1-linux-amd64) was used to again resample both images to a finer resolution.

Pixel spacing in x and y direction are equal. The z-axis, which lies approximately parallel to the phantom’s rods, has a different pixel spacing. Overall image resolution could have a significant effect on the results. Therefore all calculations were made using

original and interpolated (increased resolution) scans. See table 2.4 for more details. Figure 2.4 depicts 3 CT/MRI scans of a single rod (axial) with different resolutions. “x1” stands for the original CT scan resolution (MRI resampled to match). “x9” is a resolution resulting in 1 pixel being splitted in 9 smaller pixels, “x100” in 100, and so on. For better visibility images are printed with inverted colors. Dark pixels have a high density/intensity value, white pixels are equivalent to air (low density/intensity).

resample factor	z (not affected)	y (same as x)	x
x1	0.60	0.99	0.98
x4	0.60	0.49	0.49
x9	0.60	0.33	0.33
x25	0.60	0.2	0.2
x100	0.60	0.2	0.1

Table 2.4: pixel Spacing (rounded values) [mm]

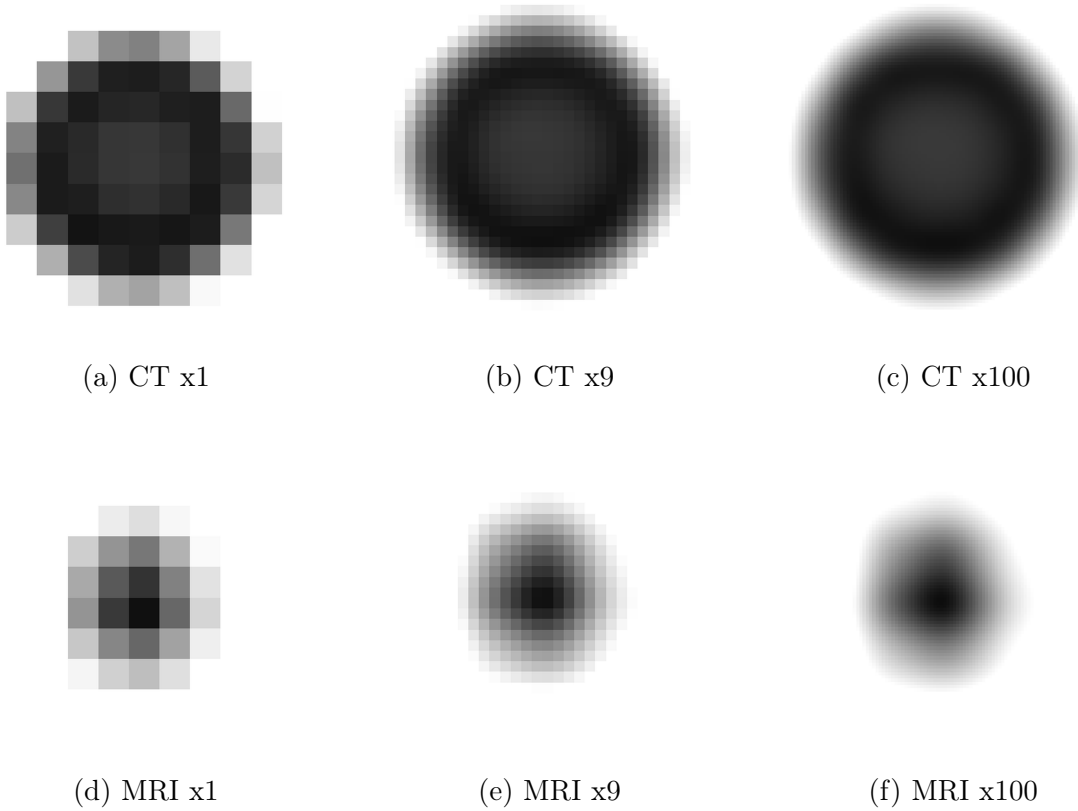


Figure 2.4: CT/MRI: axial image of single rod, filling #5 (inverted colours)

2.4.2 Capabilities

The developed software tool is not able to automatically detect individual rods shown in a CT or MRI scan. Instead the acquired 3D images have to be cropped to depict only a single rod.

The python script can:

- denoise the image data
- find the brightness values of the rod, enabling it to
- separate pixels representing the rod from surrounding air (masking)
- calculate the centroid coordinates along the rod, used to
 - location shift
 - dice coefficient (roundness/deformation)
- plot individual rod slices
 - overlaying one or two centroid coordinates
 - and save it as “.png” file
- change the pixel values to reflect the distortion occurring along a rod (visualization)
- write the calculated numbers to a “.txt” file

2.4.3 Measuring distortion

Two phenomena were chosen to reflect the amount of distortion occurring in MRI scans:

- 1) location shift (“warp”)
- 2) deformation (deviation from circular profile “DC”)

Since the rods have a cylindrical shape, distortion can only be assessed in radial direction. To make calculations easier, the z-coordinate was put parallel to the rods, x and y radial. Each slice ($z = \text{const.}$) should ideally depict the bright circular profile of the liquid (+ plastic rod in CT) surrounded by black (air). To calculate the location shift between rods shown in CT and MRI, the coordinates of the center of mass (COM) were subtracted. The location difference in each slice is saved as an array. Additionally, the absolute value of the coordinate shift (absCS) could be calculated.

The dice-coefficient “DC” (also known as Sorensen-Index) was chosen as indicator for the deviation from a circular profile. Again this value was calculated for every slice using either the CT or MRI scans.

To get a idea of the occuring distortion one should look at both the absolute value of

coordinate shift and the dice-coefficient (DC). The DC ranges from 0 to 1. A value of 1 indicates a perfect circular shape. A low DC on the other hand could be caused by many things such as: little overlap (e.g. a ring or crescent shape); a very dark image hindering delineation of rod from background; a small circle with a radius close to a only a few pixels.

2.4.4 Calculation: dice-coefficient (DC)

The dice coefficient or Sorensen index [32] is defined as:

$$DC = \frac{2|A \cap B|}{|A| + |B|} \quad (2.1)$$

The implementation into python is based on the open source python package “Medpy”. [30] A part of it’s module called “metric” was adapted. [31] All pixels above a certain threshold will be counted as input A. The reference B is a circle whose midpoint is placed at the COM.

The calculation of the DC is done by comparing an binary image to a circle. The position of the circle’s centre and its radius is highly influencing the outcome. Both the circle’s centre and its radius were varied during the distortion assesment.

2.4.5 Calculation: center of mass (COM)

The calculation of the COM is done with help of the “scipy” python package. It’s module “ndimage” contains the function “*center_of_mass()*”, which returns the COM’s coordinates of a given input array. The values assigned to voxels in CT images lie in the range from -1024 HU (air) to around 200 HU (plastic rod). Before a meaningful result can be obtained, the values need to be shifted to be > 0 . Additionally, only pixels representing the rod or the liquid should be used for the calculation. Otherwise the almost black voxels surrounding the rod would influence the result. This error could be observed especially if the rod is not placed in the exact middle of the scan. As described earlier, the plastic rod is only visible in CT images. On the MRI scans solely the liquid contained in the rods is shown. Therefore rods appear to be smaller on the MRI data. To find the relevant pixels two algorithms were developed:

- 1 calculating the number of pixels based on rod size

2 finding a COM resulting in good DC

add 1: The inner ($4mm$) and outer ($8mm$) diameter of the rods are known. So is the *pixel spacing* which represents the equivalent size of a voxel in mm . Calculating the number of pixels which make up the more or less circular profile of the rod in each slice is calculated like this:

$$pixelNumber = (radius^2 \cdot \pi) / (spacing^2) \quad (2.2)$$

For CT images $radius = 4mm$, in MRI scans $radius = 2mm$. *spacing* is the pixel spacing in x and y direction. Next the pixels are sorted by brightness. The top *pixelNumber* pixels are then used to calculate the COM.

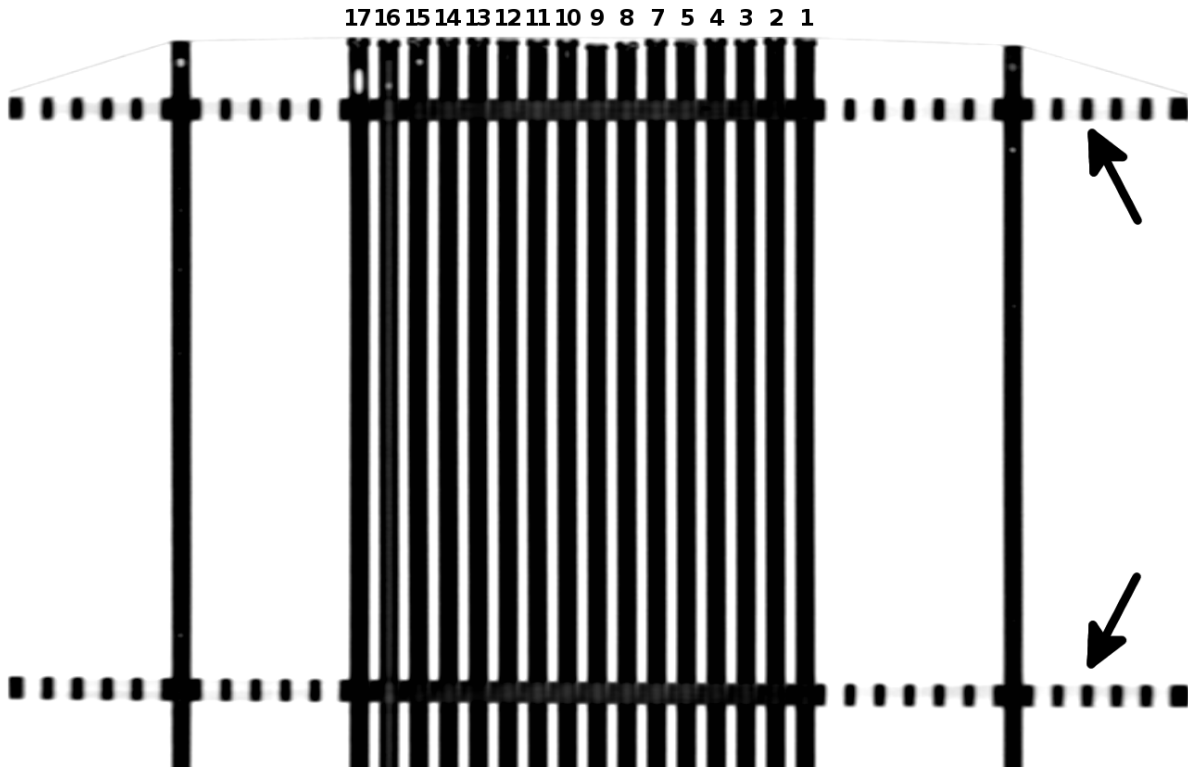
add 2: This algorithm is a iteration method. It starts by assuming $\approx 50\%$ of all pixels in the image are part of the rod. This first guess of 50% is shifted by multiplying it with $(1 \pm 0.2) \rightarrow 1.2$ and 0.8 . So in the first step two possible COMs are obtained using the brightest $50 * 1.2 = 60\%$ and $50 * 0.8 = 40\%$ of all pixels. It takes note of the values assigned to the darkest and brightest pixels used during both calculations. Those values are then set as threshold for the DC coefficient. Effectively it finds COM and DC for 52% and 60% . If the DC for using 52% is bigger, it chooses $(100\% + 50\%)/2 = 75\%$ as next guess. If on the other hand the DC for 40% is bigger, it chooses $(0\% + 50\%)/2 = 25\%$ as next guess. In the second iteration it now again shifts the percentage by multiplying it with 1.2 and 0.8 . Again COM and DC are calculated and the next guess is chosen by comparing the DCs. This is continued until the DC value decreases compared to DC found in prior steps. The maximum DC is used as indicator for the best COM.

3 Results

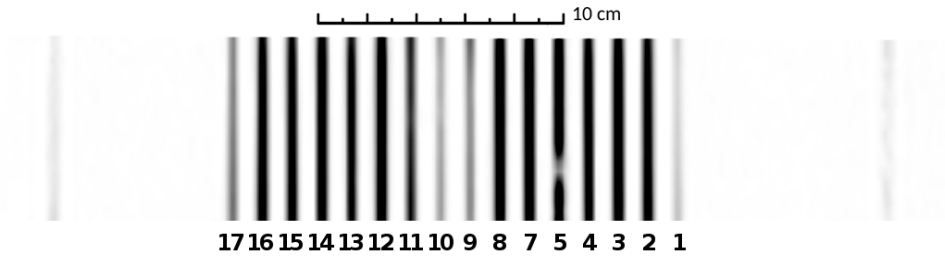
On the second day of working with the filled rods the one containing liquid #6 broke (leakage). It happened when delicately knocking it against on the table while standing upright. This was intended to mobilise bubbles that sticked to the wall and make them travel vertically to on end of the rod. (see tabular 3.2) The plasic stopper on the lower end came loose. The rod containing filling #6 was not replaced. Consequently, all CT and MRI images show only 16 rods.

3.1 Obtained MRI and CT scans

Figure 3.1 shows a coronal view of the 16 rods filled with the tested liquids. (in figure 3.2b a plasic bottle filled with water has been placed there instead (see figure 2.2).)

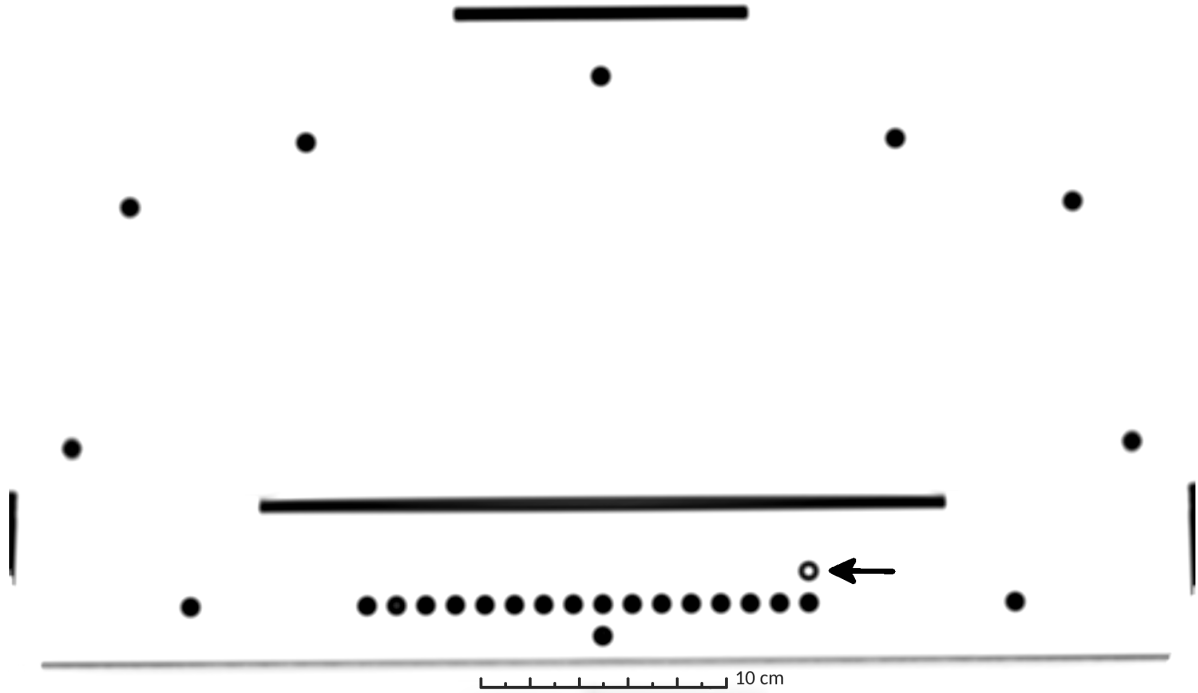


(a) CT: periodic black lines in upper and lower part of image (arrows) show plastic panes from above; rods have been fixed with adhesive tape (faint line across upper end of rods); differences in signal intensity (brightness) hardly noticeable, but air bubbles visible at upper end

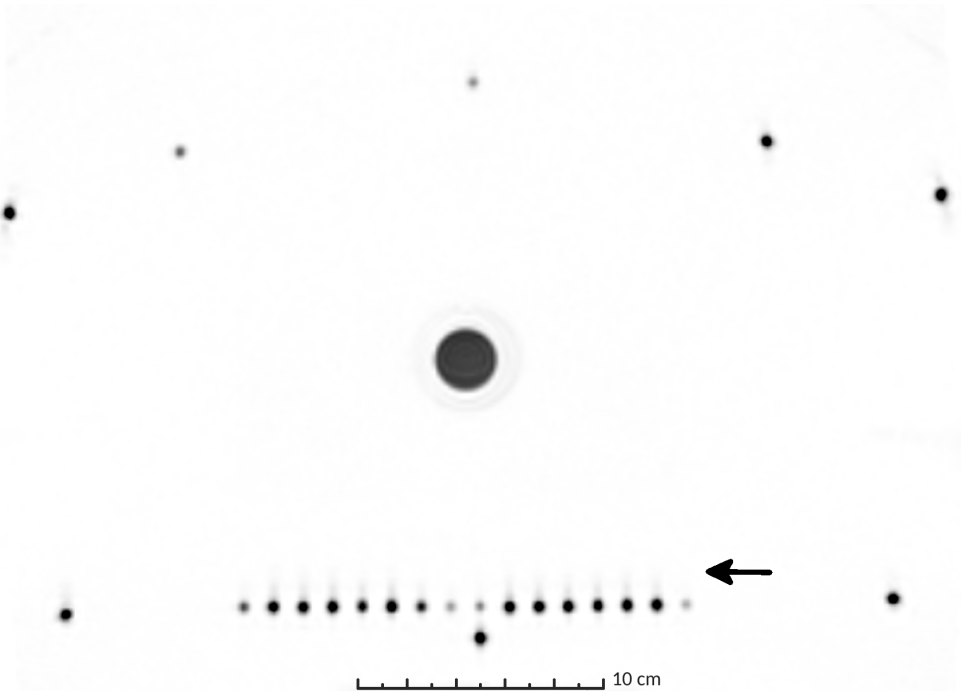


(b) MR: rods appear to be thinner, because only the liquid filling is visible; plastic (rods and panes) are not visible

Figure 3.1: Coronal CT/MRI (inverted colours; same scale; cropped images): images of 16 rods (tested liquids, numbering starting from the right, #6 excluded) + 2 reference rods (filled with water) on the sides; liquids result in different signal intensity (brightness)



(a) CT: black bars just above tested rods, at the very top and to the sides show plastic parts of the phantom holding it together; faint grey line below tested rods shows table on which phantom was positioned during imaging



(b) MRI: black circle in middle shows water bottle which was placed in the middle of the phantom (necessary for MRI scanner to start imaging)

Figure 3.2: axial CT/MRI (inverted colours, same scale): images of 16 rods (tested liquids, numbering starting from the right, #6 excluded); surrounded by reference rods (filled with water) and one empty rod (marked with arrow) which is not visible on MRI scans

3.2 Tested solutions

3.2.1 Visibility on CT/MRI scans

Generally, imaging techniques aims for a high signal-to-noise ratio. Therefore, Liquids resulting in brighter pixels are favoured.

CT images show little differences between the tested liquids. The plastic rods themselves result in brighter pixels than any of the tested solutions.

On MRI scans most liquids had a mean and a max brightness value above 1000 (see table 3.1).

Only #1, #9, #10, & #17 resulted in significantly less signal.

3.2.2 Mechanical properties of solutions

A suitable filling would yield good image contrast in CT and MRI and acceptable mechanical properties.

The liquids were filled in a rod each and observed for several months. Some solutions produced air bubbles, which would eventually lead to incorrect calculations. Each rod was free of bubbles after sealing. The amount of gas inside the rods was measured after 2 months. Ideally, tilting the entire phantom slightly should be enough to fix all rods in the phantom at the same time. In some of the tested rods the produced air bubbles would stick to the wall. Only after gently hitting the rod they would start moving (see table 3.2).

Knowing the inner diameter d of the rods we can easily approximate the volume of gas trapped:

$$V = \frac{d^2}{4} \cdot \pi \cdot l \quad (3.1)$$

Nr.	Min	Max	Mean	Median	RMS	σ
1	182	371	288	269	296,3	69,8
2	1044	1921	1443,8	1405	1477,3	312,9
3	941	2075	1451,2	1394,5	1508,9	413,2
4	1176	1709	1440	1437,5	1458,6	232,5
5	1125	2111	1583,8	1549,5	1623	355
7	971	2241	1466,8	1316	1540,6	471,2
8	1459	1947	1704	1705	1713,5	180,5
9	385	584	486,8	489	495,6	93
10	247	502	343,6	266	361,1	111
11	830	1268	1036,2	1023,5	1049	163,2
12	1158	2211	1648,8	1613	1695,2	394,2
13	836	1657	1146,8	1047	1190,9	321,2
14	800	2062	1383	1335	1461,7	473,1
15	1156	1829	1476,2	1460	1501,2	272,7
16	1102	1967	1509	1483,5	1543,8	325,8
17	356	938	629,6	602	668,1	223,6

Table 3.1: liquid visibility on MRI scan

Nr.	<i>after 1 day</i>		<i>after 2 days</i>		<i>after 1 week</i>	
	bubbles	hit req.	bubbles	hit req.	bubbles	hit req.
#1	yes	no	no		no	
#2	yes	yes	no		no	
#3	yes	yes	no		no	
#4	yes	yes	no		no	
#5	yes	no	yes	no	no	
#6	yes	no	<i>rod was leaking</i>			
#7	yes	no	yes	no	yes	no
#8	no		no		no	
#9	no		no		no	
#10	no ¹		yes	yes	yes	yes
#11	no		yes,	<i>sticked to wall</i>	yes	yes
#12	yes	yes	yes,	<i>sticked to wall</i>	yes	yes
#13	yes	yes	yes,	<i>sticked to wall</i>	yes	yes
#14	no		yes	no	yes	yes
#15	no		no		no	
#16	no		no		no	
#17	no		no		no	

Nr.	<i>after 2 months</i>	
	length of trapped bubble l [mm]	approx. volume V [mm ³]
#1	2	25.13
#2	1.8	22.62
#3	1+1 (air blockage, at lower end)	25.13
#4	4	50.27
#5	1.5 (many small bubbles)	18.85
#6	<i>rod was leaking</i>	
#7	2 (many small bubbles)	25.13
#8	2.3	28.90
#9	3	37.70
#10	2.4	30.16
#11	2	25.13
#12	2	25.13
#13	2.3	28.90
#14	1.5+0.5 (big imobile bubble, at center)	25.13
#15	3.4 (agar gel dried)	42.73
#16	0	0.00
#17	0.5	6.28

Table 3.2: solutions, observations

3.3 Distortion assesment

All results were obtained by manually cropping the 3D image to depict only a single rod.

3.3.1 Distortion

table showing distrortion along z axis (isocentre to image border)

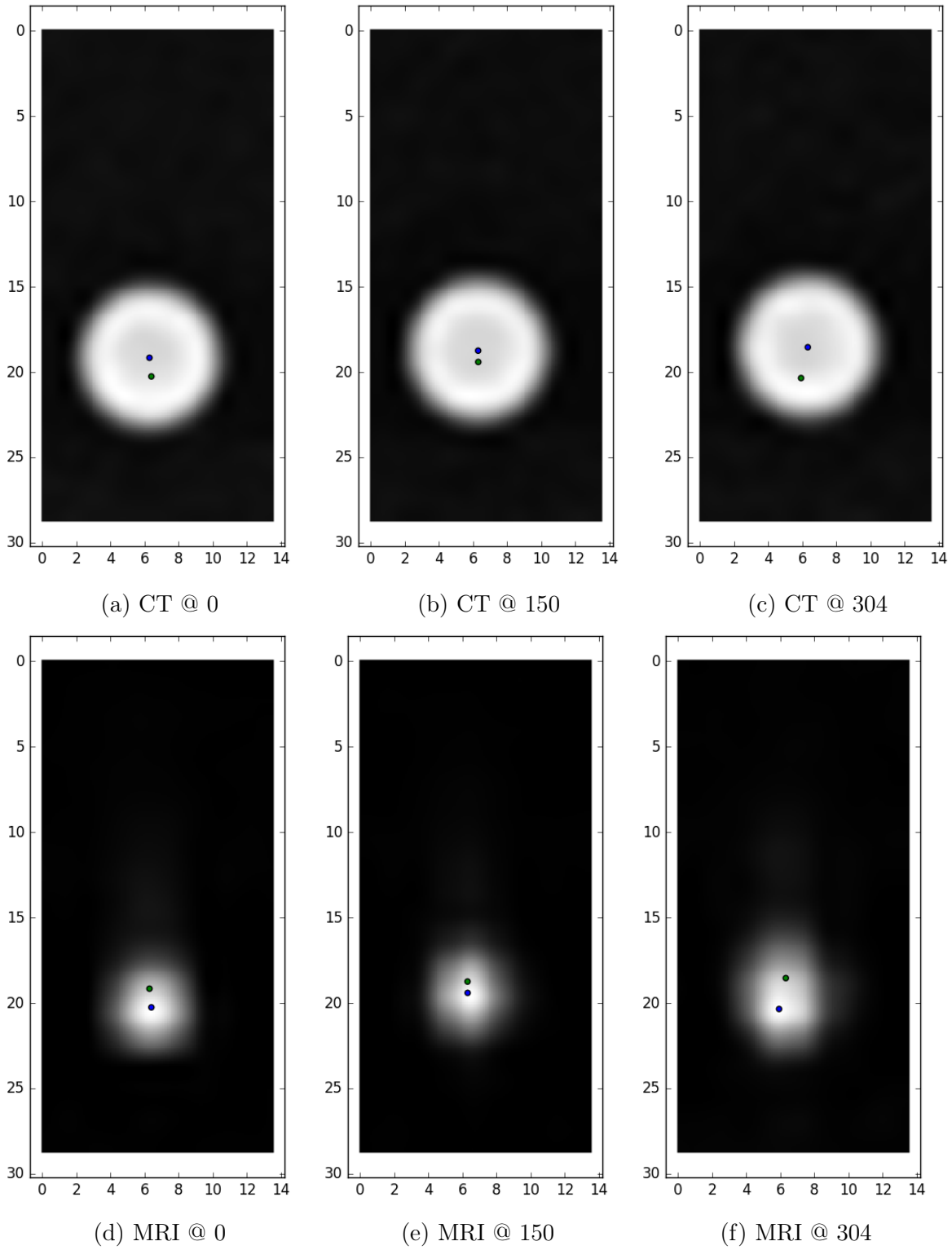


Figure 3.3: MRI x100; blue dot centroid MRI, green dot centroid CT (same scale); slice 150 is approximately at the isocentre, 0 on the very end of the image, 304 close to an air bubble

3.3.2 DC

The obtained dice coefficient varies not only because of the circle's centre and the radius, it also depends on the images resolution. Figure 3.8 and 3.9 show the DC (optimised) obtained using CT and MRI scans over resample rate.

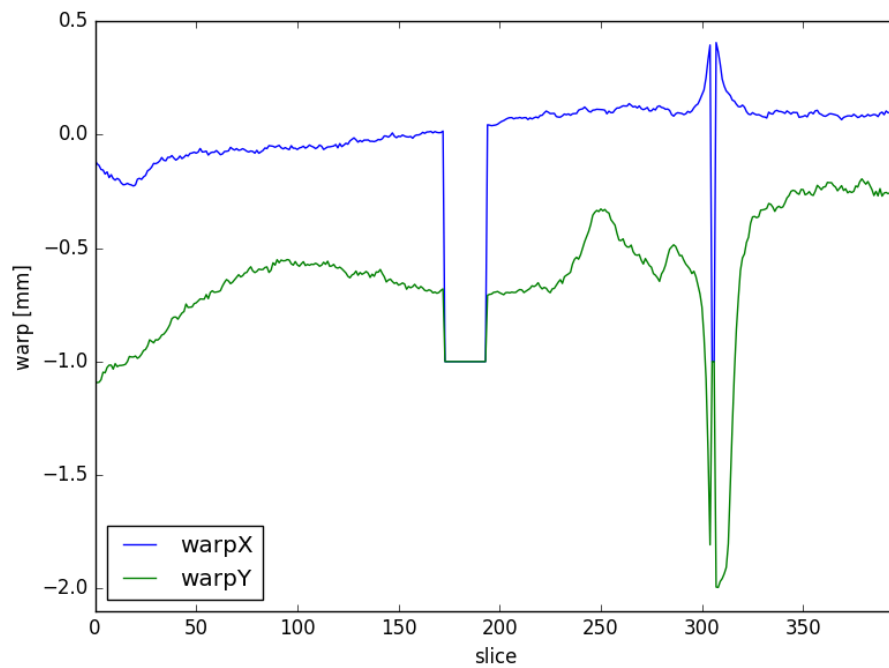


Figure 3.4: warp XY [mm], CT-MRI x100

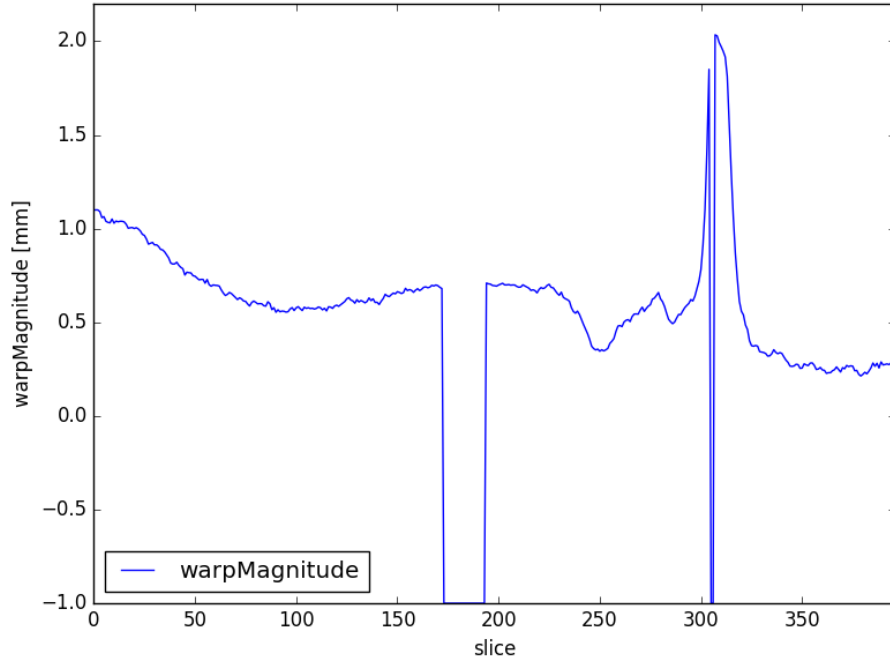


Figure 3.5: warp Magnitude [mm], CT-MRI x100

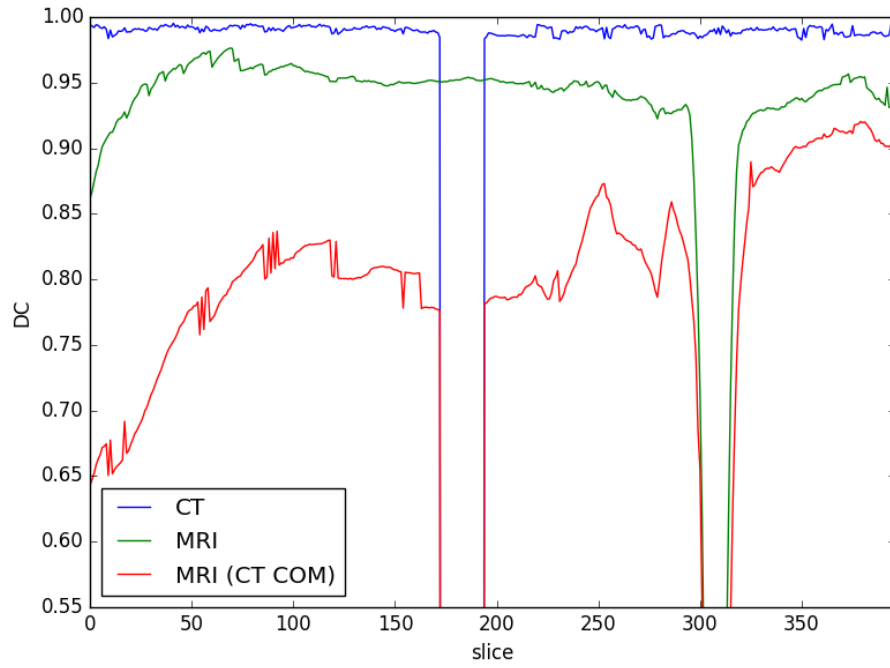


Figure 3.6: DC (optimised) for CT & MRI & MRI (using CT COM)

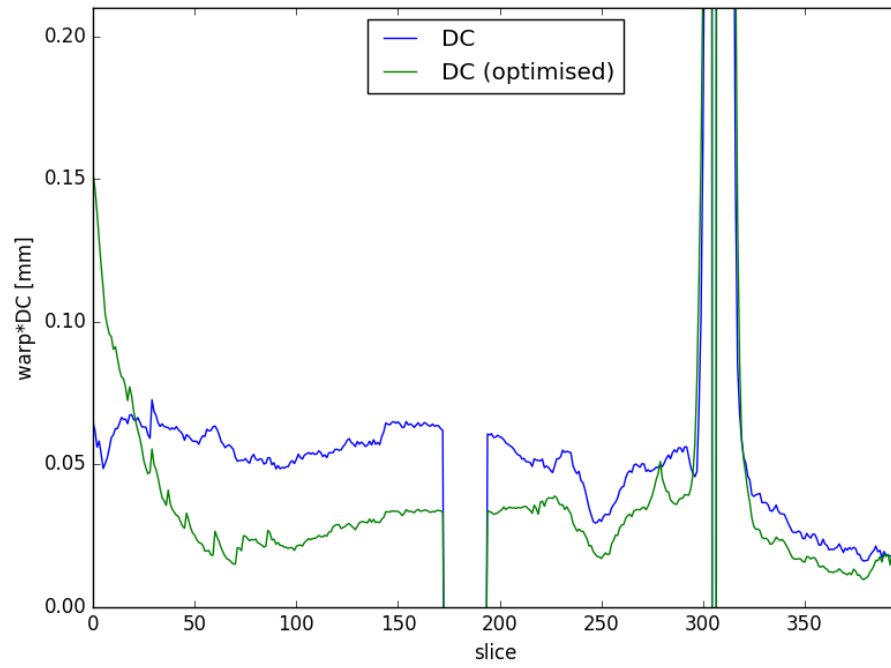


Figure 3.7: artificial indicator warp*DC using real DC and optimised DC of MRI x100

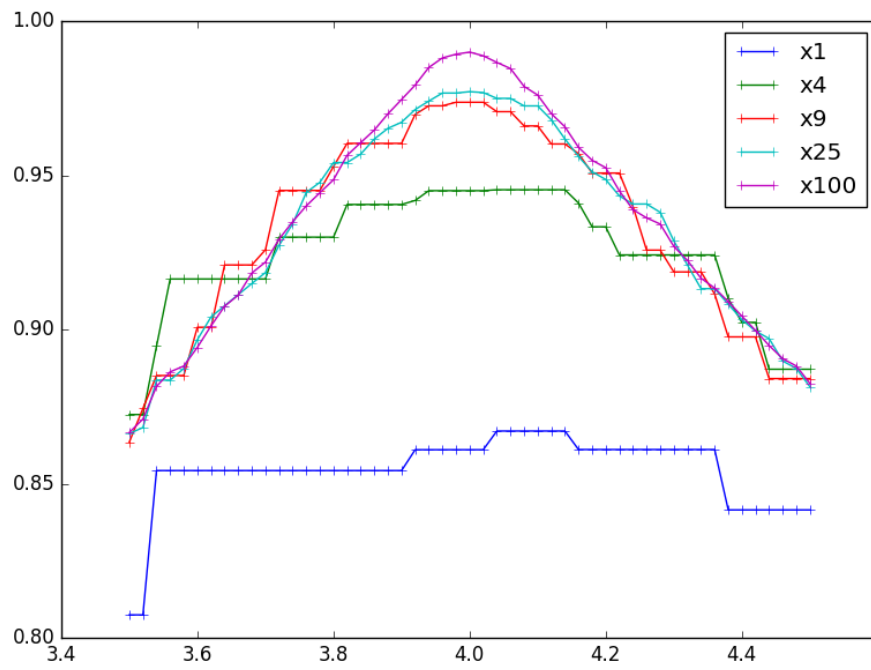
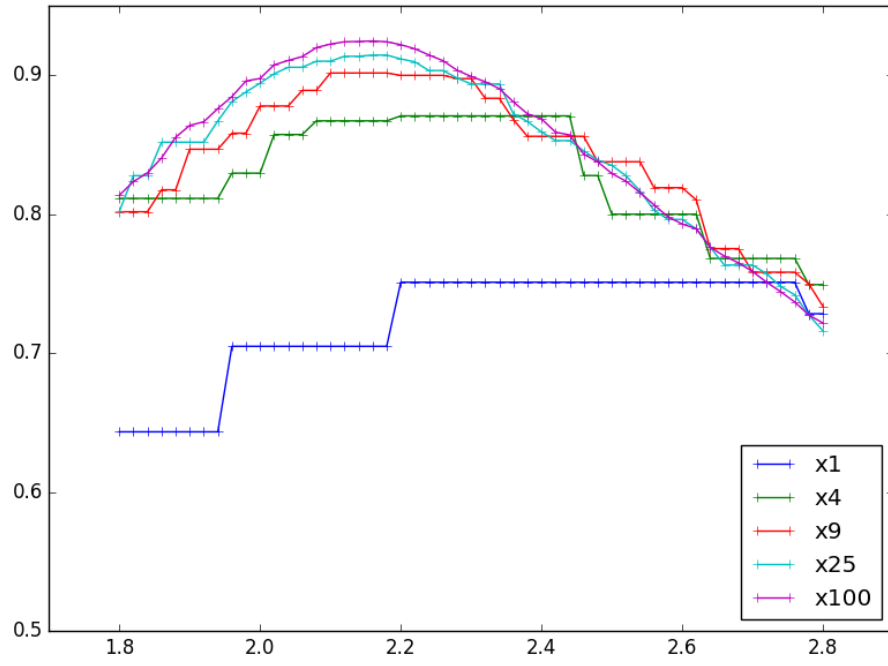
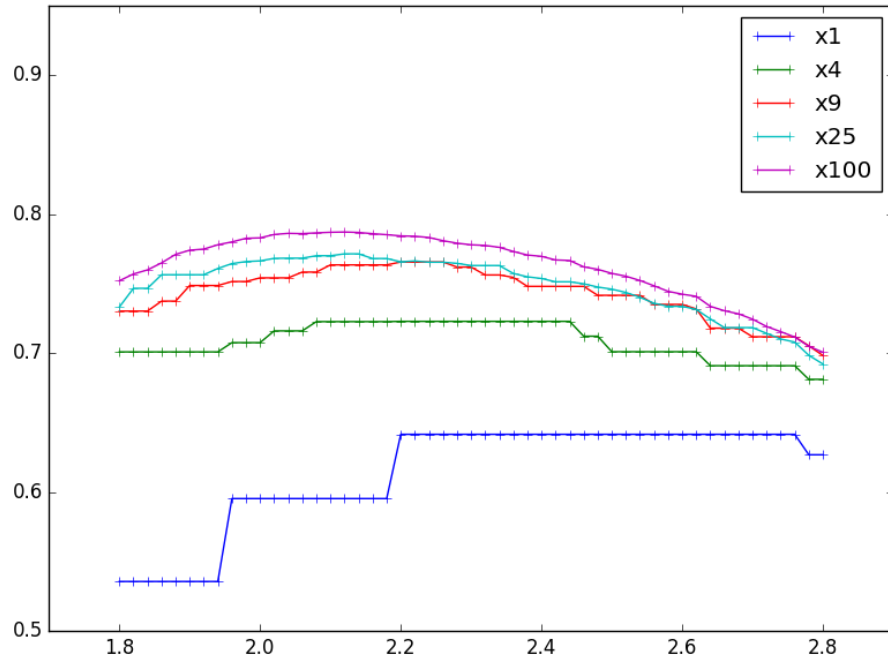


Figure 3.8: CT: DC of varied radii & resolutions



(a) MRI: DC of varied radii & resolutions



(b) MRI: DC of varied radii & resolutions (using CT-COM)

Figure 3.9

4 Discussion

4.1 Tested solutions

For measuring the position of the rods in the CT scans the plastic rods without filling would be enough already, they would not be visible on the MRI scans, though.

Oil generally shows good visibility in CT and MRI scans and produces no air bubbles after closing. However, filling all rods of the phantom with Oil is considered the last option. Water based liquids prove to be easier to clean. Since topping up over 300 rods regularly is too time consuming, oil seems to be a good alternative. However, if air bubbles could be easily shifted towards one end of the rod by tilting it slightly, they would lie outside the MRI scanner's field of view. Consequently, it would be sufficient to move air bubbles to one end of the rod before imaging.

4.2 Distortion

An air bubble might lead to an incorrect COM. Without looking at the dice-coefficient it's hard to tell why this distortion only appears to be present in a few slices. If both indicators show unexpected local irregularities, a conclusion might be easier to draw.

5 Conclusion and Outlook

5.1 Preparing the phantom for distortion assesment

5.2 Future improvement of software tool

Future improvements of the developed software tool are supposed to:

- find and register all individual rods automatically
- calculate the local distortion
- create a 3D vector map

Bibliography

- [1] *3D Slicer*. \url{https://www.slicer.org/}.
- [2] S. M. Abtahi, Majid Shahriari, M. H. Zahmatkesh, H. Khalafi, Sh Akhlaghpour, and S. Bagheri. “A new approach to contrast enhancement in MAGICA gel dosimeter image with MRI technique”. In: *Iranian Journal of Radiation Research* 6.3 (2008), pp. 151–156. ISSN: 17284562.
- [3] Christopher Bangard, Jennifer Paszek, Frank Berg, Gesa Eyl, Josef Kessler, Klaus Lackner, and Axel Gossmann. “MR imaging of claustrophobic patients in an open 1.0 T scanner: Motion artifacts and patient acceptability compared with closed bore magnets”. In: *European Journal of Radiology* 64.1 (2007), pp. 152–157. ISSN: 0720048X. DOI: 10.1016/j.ejrad.2007.02.012.
- [4] Richard S. Bodannes and Phillip C. Chan. “Ascorbic acid as a scavenger of singlet oxygen”. In: *FEBS Letters* 105.2 (1979), pp. 195–196. ISSN: 00145793. DOI: 10.1016/0014-5793(79)80609-2. URL: [http://doi.wiley.com/10.1016/0014-5793\(79\)80609-2](http://doi.wiley.com/10.1016/0014-5793(79)80609-2).
- [5] D. J. Brenner, C. D. Elliston, E. J. Hall, and W. E. Berdon. “Estimated risks of radiation-induced fatal cancer from pediatric CT”. In: *American Journal of Roentgenology* 176.2 (2001), pp. 289–296. ISSN: 0361803X. DOI: 10.2214/ajr.176.2.1760289. arXiv: 01/1762â$#36;289 [0361-803X].
- [6] M L Bucciolini Ciralo and B Lehmann. “SIMULATION OF BIOLOGIC TISSUES BY USING AGAR GELS AT MAGNETIC RESONANCE IMAGING”. In: *Acta Radiologica* 30.6 (1989).
- [7] Lili Chen, Robert A. Price, Lu Wang, Jinsheng Li, Lihong Qin, Shawn McNeeley, C. M Charlie Ma, Gary M. Freedman, and Alan Pollack. “MRI-based treatment planning for radiotherapy: Dosimetric verification for prostate IMRT”. In: *International Journal of Radiation Oncology Biology Physics* 60.2 (2004), pp. 636–647. ISSN: 03603016. DOI: 10.1016/j.ijrobp.2004.05.068.

- [8] Aaron M. Coffey, Milton L. Truong, and Eduard Y. Chekmenev. “Low-field MRI can be more sensitive than high-field MRI”. In: *Journal of Magnetic Resonance* 237 (2013), pp. 169–174. ISSN: 10960856. DOI: 10.1016/j.jmr.2013.10.013. arXiv: NIHMS150003.
- [9] C Constantinou, J C Harrington, and L a DeWerd. “An electron density calibration phantom for CT-based treatment planning computers.” In: *Medical physics* 19.2 (2012), pp. 325–327. ISSN: 00942405. DOI: 10.1118/1.596862.
- [10] Stuart Currie, Nigel Hoggard, Ian J Craven, Marios Hadjivassiliou, and Iain D Wilkinson. “Understanding MRI: basic MR physics for physicians.” In: *Postgraduate medical journal* 89.1050 (2013), pp. 209–23. ISSN: 1469-0756. DOI: 10.1136/postgradmedj-2012-131342. URL: <http://www.ncbi.nlm.nih.gov/pubmed/23223777>.
- [11] Data Spectrum Corporation. *Frequently Asked Questions - How do I eliminate air bubbles in the Mini, Micro and Ultra Micro line of phantoms?* \url{http://www.spect.com/faq.html}.
- [12] Marc Debois, Raymond Oyen, Frederik Maes, Geert Verswijvel, Giovanna Gatti, Hilde Bosmans, Michel Feron, Erwin Bellon, Gerald Kutcher, Hein Van Poppel, and Luc Vanuytsel. “The contribution of magnetic resonance imaging to the three-dimensional treatment planning of localized prostate cancer”. In: *International Journal of Radiation Oncology Biology Physics* 45.4 (1999), pp. 857–865. ISSN: 03603016. DOI: 10.1016/S0360-3016(99)00288-6. URL: <http://www.sciencedirect.com/science/article/pii/S0360301699002886>.
- [13] *DICOM: About DICOM*. \url{http://dicom.nema.org/Dicom/about-DICOM.html}. URL: <http://dicom.nema.org/Dicom/about-DICOM.html> (visited on 01/08/2017).
- [14] Jeff H. Duyn. *The future of ultra-high field MRI and fMRI for study of the human brain*. 2012. DOI: 10.1016/j.neuroimage.2011.10.065. arXiv: NIHMS150003.
- [15] Judith Enders, Elke Zimmermann, Matthias Rief, Peter Martus, Randolph Klingebiel, Patrick Asbach, Christian Klessen, Gerd Diederichs, Moritz Wagner, Ulf Teichgraber, Thomas Bengner, Bernd Hamm, and Marc Dewey. *Reduction of claustrophobia with short-bore versus open magnetic resonance imaging: A randomized controlled trial*. 2011. DOI: 10.1371/journal.pone.0023494.
- [16] Alice R. Goldman and Pierre D. Maldjian. *Reducing radiation dose in body CT: A practical approach to optimizing CT protocols*. 2013. DOI: 10.2214/AJR.12.10330.

- [17] Peter Greer, D Ph, Jason Dowling, D Ph, Peter Pichler, Jidi Sun, M Sc, Haylea Richardson, B Med Rad Sc, David Rivest-henault, D Ph, Soumya Ghose, D Ph, Jarad Martin, Chris Wratten, Jameen Arm, Leah Best, Jim Denham, and Peter Lau. “Development of MR-only Planning for Prostate Radiation Therapy Using Synthetic CT”. In: (2015), pp. 61–62.
- [18] Alexandra Hellerbach, Verena Schuster, Andreas Jansen, and Jens Sommer. “MRI Phantoms – Are There Alternatives to Agar?” In: *PLoS ONE* 8.8 (2013). DOI: 10.1371/.
- [19] William Henry. “Experiments on the Quantity of Gases Absorbed by Water, at Different Temperatures, and under Different Pressures”. In: *Philosophical Transactions of the Royal Society of London* 93.1 (1803), pp. 29–274. ISSN: 02610523. DOI: 10.1098/rstl.1803.0004. URL: http://www.jstor.org/stable/107068?seq=1{\#}page{_}scan{_}tab{_}contents.
- [20] J. D. Hunter. *Matplotlib: A 2D graphics environment*. \url{http://matplotlib.org/}. 2007. DOI: 10.1109/MCSE.2007.55.
- [21] Edward F Jackson. “MR Acceptance Testing and Quality Control : Previous MR Committee TG Reports MRI Acceptance Testing - E . Jackson Levels of Involvement MR Acceptance Test Reality Check MR Siting Issues”. In: 17.1 (2009), pp. 287–295.
- [22] Edward F. Jackson, Michael J. Bronskill, Dick J. Drost, Joseph Och, Wlad T. Sobol, and Geoffrey D. Clarke. *AAPM Report No. 100 Acceptance Testing and Quality Assurance Procedures for Magnetic Resonance Imaging Facilities Report of MR Subcommittee Task Group I*. 100. 2010, pp. 1–32. ISBN: 9781936366026.
- [23] R Kikinis. *Overview: functions of 3D Slicer*. \url{http://perk.cs.queensu.ca/sites/perk.cs.queensu.ca/files/04-30-Kikinis-Slicer-reduced.pdf}. 2012.
- [24] Adamos Kyriakou. *DICOM in Python: Importing medical image data into NumPy with PyDICOM and VTK*. \url{https://pyscience.wordpress.com/2014/09/08/dicom-in-python-importing-medical-image-data-into-numpy-with-pydicom-and-vtk/}. (Visited on 01/10/2017).
- [25] Adamos Kyriakou. *Image Segmentation with Python and SimpleITK*. \url{https://pyscience.wordpress.com/2014/09/08/image-segmentation-with-python-and-simpleitk/}.

- [26] Tuong Le. “High-field, high-performance magnetic resonance: Technical challenges and clinical applications”. In: *The journal of practical medical imaging and management* (2004), pp. 1–8.
- [27] A.D.A Maidment and M.J Yaffe. “Mammography”. In: *Diagnostic Radiology Physics A Handbook for Teachers and Students* (2014), pp. 209–235.
- [28] R Mathur-De Vre, R Grimee, F Parmentier, and J Binet. “The use of agar gel as a basic reference material for calibrating relaxation times and imaging parameters.” In: *Magnetic resonance in medicine : official journal of the Society of Magnetic Resonance in Medicine / Society of Magnetic Resonance in Medicine* 2.2 (1985), pp. 176–179. ISSN: 0740-3194. DOI: 10.1002/mrm.1910020208.
- [29] Cynthia H. McCollough, Andrew N. Primak, Natalie Braun, James Kofler, Lifeng Yu, and Jodie Christner. *Strategies for Reducing Radiation Dose in CT*. 2009. DOI: 10.1016/j.rc1.2008.10.006.
- [30] *MedPy 0.2.2 : Python Package Index*. \url{https://pypi.python.org/pypi/MedPy}. URL: <https://pypi.python.org/pypi/MedPy> (visited on 12/19/2016).
- [31] *medpy.metric.binary — MedPy 0.2.2 documentation*. \url{http://pythonhosted.org/MedPy/_modules/medpy/metric/binary}. URL: http://pythonhosted.org/MedPy/{_}modules/medpy/metric/binary.html{\#}dc (visited on 12/19/2016).
- [32] *medpy.metric.binary.dc — MedPy 0.2.2 documentation*. \url{http://pythonhosted.org/MedPy/generated/medpy.metric.binary.dc}. URL: <http://pythonhosted.org/MedPy/generated/medpy.metric.binary.dc.html{\#}medpy.metric.binary.dc> (visited on 12/19/2016).
- [33] Takashi Mizowaki, Yasushi Nagata, Kaoru Okajima, Masaki Kokubo, Yoshiharu Negoro, Norio Araki, and Masahiro Hiraoka. “Reproducibility of geometric distortion in magnetic resonance imaging based on phantom studies”. In: *Radiotherapy and Oncology* 57.2 (2000), pp. 237–242. ISSN: 01678140. DOI: 10.1016/S0167-8140(00)00234-6.
- [34] Martin J Murphy, James Balter, Stephen Balter, Jose a BenComo, Indra J Das, Steve B Jiang, C M Ma, Gustavo H Olivera, Raymond F Rodebaugh, Kenneth J Ruchala, Hiroki Shirato, and Fang-Fang Yin. “The management of imaging dose during image-guided radiotherapy: report of the AAPM Task Group 75.” In: *Medical physics* 34.10 (2007), pp. 4041–4063. ISSN: 00942405. DOI: 10.1118/1.2775667.

- [35] K Nakamura, E T Al., and (Particle Data Group). “Passage of particles through matter”. In: *Journal of Physics* G.37 (2010), p. 075021. ISSN: 1434-6044. DOI: and2011partialupdateforthe2012edition. (pdg.lbl.gov).
- [36] Tufve Nyholm and Joakim Jonsson. “Technical Aspects of MR-only Radiotherapy”. In: (2015), pp. 65–67.
- [37] Joseph G Och, Geoffrey D Clarke, Wladyslaw T Sobol, Coleman W Rosen Seong, Ki Mun, Coleman W Rosen, and Seong Ki Mun. “ACCEPTANCE TESTING OF MAGNETIC RESONANCE IMAGING SYSTEMS* Acceptance testing of magnetic resonance imaging systems: Report of AAPM Nuclear Magnetic Resonance Task Group No. 6 a)”. In: *Reprinted from MEDICAL PHYSICS* 19.1 (1992), pp. 271–7344. ISSN: 0094-2405. DOI: 10.1118/1.596903.
- [38] Harald Paganetti and Thomas Bortfeld. *Proton beam radiotherapy - The state of the art*. October. 2005, pp. 3–540. ISBN: 3540003215. DOI: 10.1118/1.1999671. URL: <http://www.aapm.org/meetings/05AM/pdf/18-4016-65735-22.pdf>.
- [39] Bernhard Petersch, Joachim Bogner, Annette Fransson, Thomas Lorang, and Richard Pötter. “Effects of geometric distortion in 0.2 T MRI on radiotherapy treatment planning of prostate cancer”. In: *Radiotherapy and Oncology* 71.1 (2004), pp. 55–64. ISSN: 01678140. DOI: 10.1016/j.radonc.2003.12.012.
- [40] “Physico-Chemical Properties”. In: ().
- [41] E B Podgorsak. “Radiation Oncology”. In: *Radiation Oncology* ().
- [42] Ryan G. Price, Mo Kadbi, Joshua Kim, James Balter, Indrin J. Chetty, and Carri K. Glide-Hurst. “Technical Note: Characterization and correction of gradient non-linearity induced distortion on a 1.0 T open bore MR-SIM”. In: *Medical Physics* 42.10 (2015), pp. 5955–5960. ISSN: 0094-2405. DOI: 10.1118/1.4930245. URL: <http://scitation.aip.org/content/aapm/journal/medphys/42/10/10.1118/1.4930245>.
- [43] *Pydicom*. \url{http://pydicom.readthedocs.io/en/stable/getting_started.html}. (Visited on 01/10/2017).
- [44] *Python 2.7.13*. \url{https://www.python.org/}. (Visited on 01/10/2017).

- [45] Christopher M. Rank, Nora Hünemohr, Armin M. Nagel, Matthias C. Röthke, Oliver Jäkel, and Steffen Greilich. “MRI-based simulation of treatment plans for ion radiotherapy in the brain region”. In: *Radiotherapy and Oncology* 109.3 (2013), pp. 414–418. ISSN: 01678140. DOI: 10.1016/j.radonc.2013.10.034.
- [46] Coen Rasch, Isabelle Barillot, Peter Remeijer, Adriaan Touw, Marcel Van Herk, and Joos V. Lebesque. “Definition of the prostate in CT and MRI: A multi-observer study”. In: *International Journal of Radiation Oncology Biology Physics* 43.1 (1999), pp. 57–66. ISSN: 03603016. DOI: 10.1016/S0360-3016(98)00351-4.
- [47] Mack Roach, Pamela Faillace-Akazawa, Christine Malfatti, John Holland, and Hedvig Hricak. “Prostate volumes defined by magnetic resonance imaging and computerized tomographic scans for three-dimensional conformal radiotherapy”. In: *International Journal of Radiation Oncology Biology Physics* 35.5 (1996), pp. 1011–1018. ISSN: 03603016. DOI: 10.1016/0360-3016(96)00232-5.
- [48] Martin Rohrer, Hans Bauer, Jan Mintorovitch, Martin Requardt, and Hanns-Joachim Weinmann. “Comparison of Magnetic Properties of MRI Contrast Media Solutions at Different Magnetic Field Strengths”. In: ().
- [49] B K Rutt and D H Lee. “The impact of field strength on image quality in MRI.” In: *Journal of magnetic resonance imaging : JMRI* 6.1 (1996), pp. 57–62. ISSN: 1053-1807. DOI: 3TLibrary-Converted#12;Usedtobe#1642.
- [50] R. Sander. “Compilation of Henry’s law constants (version 4.0) for water as solvent”. In: *Atmospheric Chemistry and Physics* 15.8 (2015), pp. 4399–4981. ISSN: 16807324. DOI: 10.5194/acp-15-4399-2015.
- [51] U Schneider, E. Pedroni, and Antony Lomax. “The calibration of CT Hounsfield units for radiotherapy treatment planning.” In: *Physics in medicine and biology* 41.1 (1996), pp. 111–24. ISSN: 0031-9155. DOI: 10.1088/0031-9155/41/1/009. arXiv: arXiv:1011.1669v3. URL: <http://www.ncbi.nlm.nih.gov/pubmed/8685250>.
- [52] *SimpleITK*. \url{http://www.simpleitk.org/}. (Visited on 12/19/2016).
- [53] *SimpleITK: IPython Notebooks*. \url{http://insightsoftwareconsortium.github.io/SimpleITK-Notebooks/}. (Visited on 12/19/2016).
- [54] *SimpleITK/GettingStarted - KitwarePublic*. \url{https://itk.org/Wiki/SimpleITK/GettingStarted}. URL: <https://itk.org/Wiki/SimpleITK/GettingStarted> (visited on 01/10/2017).

- [55] A. B. Smith, W. P. Dillon, R. Gould, and Max Wintermark. *Radiation dose-reduction strategies for neuroradiology CT protocols*. 2007. DOI: 10.3174/ajnr.A0814.
- [56] Aaron Sodickson, Pieter F Baeyens, Katherine P Andriole, Luciano M Prevedello, Richard D Nawfel, Richard Hanson, and Ramin Khorasani. “Recurrent CT, cumulative radiation exposure, and associated radiation-induced cancer risks from CT of adults.” In: *Radiology* 251.1 (2009), pp. 175–184. ISSN: 0033-8419. DOI: 10.1148/radiol.2511081296. URL: <http://pubs.rsna.org/doi/abs/10.1148/radiol.2511081296>.
- [57] Teodor Stanescu, Jans Hans-Sonke, Pavel Stavrev, and B. Gino Fallone. “3T MR-based treatment planning for radiotherapy of brain lesions”. In: *Radiology and Oncology* 40.2 (2006), pp. 125–132. ISSN: 13182099. URL: <http://www.scopus.com/inward/record.url?eid=2-s2.0-33746661222&partnerID=tZ0tx3y1>.
- [58] Tarraf Torfeh, Rabih Hammoud, Maeve McGarry, Noora Al-Hammadi, and Gregory Perkins. “Development and validation of a novel large field of view phantom and a software module for the quality assurance of geometric distortion in magnetic resonance imaging.” In: *Magnetic Resonance Imaging* 33.7 (2015), pp. 939–949. ISSN: 0730725X. DOI: 10.1016/j.mri.2015.04.003. URL: <http://eutils.ncbi.nlm.nih.gov/entrez/eutils/elink.fcgi?dbfrom=pubmed&id=25882440&retmode=ref&cmd=prlinks&5Cnpapers3://publication/doi/10.1016/j.mri.2015.04.003http://eutils.ncbi.nlm.nih.gov/entrez/eutils/elink.fcgi?dbfrom=pubmed&7B&7Ddid=25882440&7B&7Dretmode=re>.
- [59] Bernard E. Van Beers, Catherine M. Pastor, and Hero K. Hussain. *Primovist, eovist: What to expect?* 2012. DOI: 10.1016/j.jhep.2012.01.031.
- [60] Hitoshi Wada, Masaki Sekino, Hiroyuki Ohsaki, Tatsuhiro Hisatsune, Hiroo Ikehira, and Tsukasa Kiyoshi. “Prospect of high-field MRI”. In: *IEEE Transactions on Applied Superconductivity*. Vol. 20. 3. 2010, pp. 115–122. ISBN: 1051-8223. DOI: 10.1109/TASC.2010.2043939.
- [61] Amy Walker, Gary Liney, Lois Holloway, Jason Dowling, David Rivest-Henault, and Peter Metcalfe. “Continuous table acquisition MRI for radiotherapy treatment planning: Distortion assessment with a new extended 3D volumetric phantom.” In:

Medical physics 42.4 (2015), p. 1982. ISSN: 0094-2405. DOI: 10.1118/1.4915920.
URL: <http://www.ncbi.nlm.nih.gov/pubmed/25832089>.

- [62] Deming Wang, David M. Doddrell, and Gary Cowin. “A novel phantom and method for comprehensive 3-dimensional measurement and correction of geometric distortion in magnetic resonance imaging”. In: *Magnetic Resonance Imaging* 22.4 (2004), pp. 529–542. ISSN: 0730725X. DOI: 10.1016/j.mri.2004.01.008.
- [63] Deming Wang, Wendy Strugnell, Gary Cowin, David M. Doddrell, and Richard Slaughter. “Geometric distortion in clinical MRI systems: Part II: Correction using a 3D phantom”. In: *Magnetic Resonance Imaging* 22.9 (2004), pp. 1223–1232. ISSN: 0730725X. DOI: 10.1016/j.mri.2004.08.014.